The Cocoon Shocks of Cygnus A: Pressures and Their Implications for the Jets and Lobes

Journal Item

The Astrophysical Journal, 855:71 (15pp), 2018 March 1 https://doi.org/10.3847/1538-4357/aaaf1a

The Cocoon Shocks of Cygnus A: Pressures and Their Implications for the Jets and Lobes

Bradford Snios[1], Paul E. J. Nulsen[1,2], Michael W. Wise[3,4], Martijn de Vries[4], Mark Birkinshaw[5], Diana M. Worrall[5], Ryan T. Duffy[5], Ralph P. Kraft[1], Brian R. McNamara[6], Chris Carilli[7], Judith H. Croston[8], Alastair C. Edge[9], Leith E. H. Godfrey[3], Martin J. Hardcastle[10], Daniel E. Harris[1,14], Robert A. Laing[11], William G. Mathews[12], John P. McKean[3], Richard A. Perley[7], David A. Rafferty[13], and Andrew J. Young[5]

[1] Harvard-Smithsonian Center for Astrophysics, 60 Garden Street, Cambridge, MA 02138, USA
[2] ICRAR, University of Western Australia, 35 Stirling Hwy, Crawley, WA 6009, Australia
[3] ASTRON (Netherlands Institute for Radio Astronomy), P.O. Box 2, 7990 AA Dwingeloo, The Netherlands
[4] Astronomical Institute "Anton Pannekoek," University of Amsterdam, Postbus 94249, 1090 GE Amsterdam, The Netherlands
[5] H. H. Wills Physics Laboratory, University of Bristol, Tyndall Ave, Bristol BS8 1TL, UK
[6] Department of Physics & Astronomy, University of Waterloo, 200 University Avenue, West Waterloo, Ontario N2L 3G1, Canada
[7] National Radio Astronomy Observatory, P.O. Box 0, Socorro, NM 87801, USA
[8] School of Physical Sciences, The Open University, Walton Hall, Milton Keynes, MK6 7AA, UK
[9] Department of Physics, University of Durham, South Road, Durham, DH1 3LE, UK
[10] School of Physics, Astronomy and Mathematics, University of Hertfordshire, College Lane, Hatfield, Hertfordshire AL10 9AB, UK
[11] Square Kilometre Array Organisation, Jodrell Bank Observatory, Lower Withington, Macclesfield, Cheshire SK11 9DL, UK
[12] UCO/Lick Observatory, Department of Astronomy and Astrophysics, University of California, Santa Cruz, CA 95064, USA
[13] Hamburger Sternwarte, Universität Hamburg, Gojenbergsweg 112, D-21029, Hamburg, Germany
Received 2018 January 11; revised 2018 February 7; accepted 2018 February 9; published 2018 March 8

Abstract

We use 2.0 Msec of *Chandra* observations to investigate the cocoon shocks of Cygnus A and some implications for its lobes and jet. Measured shock Mach numbers vary in the range 1.18–1.66 around the cocoon. We estimate a total outburst energy of $\simeq 4.7 \times 10^{60}$ erg, with an age of $\simeq 2 \times 10^7$ years. The average postshock pressure is found to be $8.6 \pm 0.3 \times 10^{-10}$ erg cm^{-3}, which agrees with the average pressure of the thin rim of compressed gas between the radio lobes and shocks, as determined from X-ray spectra. However, average rim pressures are found to be lower in the western lobe than in the eastern lobe by $\simeq 20\%$. Pressure estimates for hotspots A and D from synchrotron self-Compton models imply that each jet exerts a ram pressure $\gtrsim 3$ times its static pressure, consistent with the positions of the hotspots moving about on the cocoon shock over time. A steady, one-dimensional flow model is used to estimate jet properties, finding mildly relativistic flow speeds within the allowed parameter range. Models in which the jet carries a negligible flux of rest mass are consistent with the observed properties of the jets and hotspots. This favors the jets being light, implying that the kinetic power and momentum flux are carried primarily by the internal energy of the jet plasma rather than by its rest mass.

Key words: galaxies: active – galaxies: clusters: general – galaxies: individual (Cygnus A) – X-rays: galaxies

Supporting material: data behind figure

1. Introduction

It is widely accepted that active galactic nuclei (AGNs) significantly affect their galaxy hosts, likely playing a central role in the formation and evolution of galaxies and larger-scale structure (e.g., Fabian 2012). For many galaxy clusters, such as those with cool cores, in the absence of a heat source, X-ray-emitting hot gas at the center would start cooling in less than 1 Gyr, at rates in excess of one hundred solar masses per year. However, in the majority of cases, a radio AGN hosted by the central galaxy deposits sufficient power via jets to prevent the gas from cooling (Bîrzan et al. 2004; Dunn & Fabian 2006; Rafferty et al. 2006; McNamara & Nulsen 2007). By limiting copious cooling and the consequent star formation at cluster centers, radio AGNs can resolve the cooling flow problem (Fabian 1994; Tabor & Binney 1993; Tucker & David 1997), account for the lack of star formation in the central galaxies, and explain the steep decline in the galaxy luminosity function at high luminosities (Bower et al. 2006; Croton et al. 2006). Similar phenomena are observed in the lower-mass halos of galaxy groups and massive elliptical galaxies that host a substantial hot atmosphere. As a result, the interaction between radio AGNs hosted by cluster central galaxies and their environments has become a central issue for structure formation.

The Fanaroff–Riley class II (FRII) radio galaxy (Fanaroff & Riley 1974) Cygnus A (Cyg A) is the archetype of powerful radio galaxies (Carilli & Barthel 1996). At a redshift of $z = 0.0561$ (Owen et al. 1997; Smith et al. 2002; Duffy et al. 2018) and with an estimated jet power approaching 10^{46} erg s^{-1} (e.g., Godfrey & Shabala 2013 and see below), it is by far the nearest truly powerful radio galaxy in the universe. Cyg A is hosted by the central galaxy of a rich, cool-core galaxy cluster (Owen et al. 1997), and X-ray observations can provide a valuable probe of the energy flows through the jets from its AGN, the interaction of the jets with the surrounding medium, and the overall system's impact on its environment (e.g., Carilli et al. 1988, 1994; Harris et al. 1994; Smith et al. 2002; Rafferty et al. 2006). X-ray observations of Cyg A also provide a unique opportunity to investigate the physical structure of a powerful radio galaxy and discuss its evolution over time. Beyond further understanding of Cyg A, analysis of

[14] Dan Harris passed away on 2015 December 6. His contributions to radio and X-ray astronomy will always be remembered.

this system is also beneficial to the study of FRII systems in general.

This paper is one of a series on the analysis and interpretation of 2.0 Msec of *Chandra* X-ray observations of Cyg A. Its focus is the cocoon shocks of Cyg A and what they tell us about the AGN outburst and the physical properties of the lobes and jets. The cocoon shocks extend from $\simeq 30''$ (33 kpc) north of the AGN, at their closest, to just beyond the western hotspot, at $\simeq 67''$ (74 kpc) from the AGN on the sky. They are driven by the momentum and power deposited by the jets (Scheuer 1974; Begelman et al. 1984; Heinz et al. 1998; Reynolds et al. 2001). In Section 2, we describe the data used and outline our method of data analysis. In Section 3, we determine the radial profiles of the properties of the intracluster medium (ICM) in sectors centered on the AGN. In Section 4, we expand upon previous works (e.g., Smith et al. 2002; Wilson et al. 2006), using X-ray surface brightness profiles to determine shock strengths at a number of locations around the periphery of the cocoon. The results rely on model-dependent assumptions, which we test by checking consistency with several alternative measures of the shock strength, based on temperature jumps, shock compression, and postshock pressures. Postshock pressures provide good estimates of the pressure within the radio lobes, away from the immediate vicinity of the hotspots, where the pressure is expected to be substantially higher than in the rest of the lobe (Scheuer 1974; Harris et al. 1994; Carilli & Barthel 1996; Blundell et al. 1999; Mathews & Guo 2012). Postshock pressures are presented in Section 5, together with pressure estimates determined from X-ray spectra for the narrow rim of compressed gas between the cocoon shock and the radio lobes. Some physical consequences of our results are discussed in Section 6. Results for the rate of expansion of the cocoon shock and a self-similar model for the inflation of the radio lobes are used to estimate the velocity of the AGN relative to the hot gas and the speed of advance of the hotspots. The fitted shock models are used to estimate the outburst energy and mean power of the jets. Lastly, estimates of the hotspot pressures from synchrotron self-Compton models are used to obtain estimates of the jet speeds.

We assume $H_0 = 69.3\ \mathrm{km\ s^{-1}\ Mpc^{-1}}$, $\Omega_M = 0.288$, and $\Omega_\Lambda = 0.712$ (Hinshaw et al. 2013), which give an angular scale for Cyg A of 1.103 kpc arcsec^{-1} and an angular diameter distance of 227 Mpc at the redshift $z = 0.0561$. The Galactic H I column density is set to $3.1 \times 10^{21}\ \mathrm{cm^{-2}}$ based on an average of the results from Dickey & Lockman (1990) and Kalberla et al. (2005). All uncertainty ranges are 68% confidence intervals, unless otherwise stated.

2. *Chandra* Data Reduction

Cyg A was initially observed by *Chandra* on 2000 May 21 (ObsID 00360) using the Advanced CCD Imaging Spectrometer (ACIS) with the object centered on the S3 chip in FAINT mode. A follow-up observation was performed with the S3 chip in VFAINT mode (ObsID 01707), and all subsequent observations were performed with ACIS-I centered on the AGN of Cyg A, its western hotspot, or its eastern hotspot (observations targeting the merging subcluster were not used). A complete list of the observations used in our analysis is given in Table 1. All data were reprocessed using CIAO 4.9, with CALDB 4.7.4 (Fruscione et al. 2006), and the routine deflare was used to remove background flares. The resulting cleaned exposure times are shown in Table 1, with a total exposure time of 1.96 Msec. Additionally, the readout_bkg routine was used to estimate the distribution of "out-of-time" events, those due to events detected during frame transfer, for each observation. The cleaned exposures, corrected for out-of-time events, were used in all of the analysis discussed in this article.

Table 1
Chandra Observations Used

ObsID	Date	$T_{\rm exp}$[a] (ks)	ObsID	Date	$T_{\rm exp}$[a] (ks)
00360	2000 May 21	34.3	17517	2016 Sep 17	26.7
01707	2000 May 26	9.2	17518	2016 Jul 16	49.4
05830	2005 Feb 22	23.5	17519	2016 Dec 19	29.6
05831	2005 Feb 16	50.6	17520	2016 Dec 06	26.8
06225	2005 Feb 15	24.3	17521	2016 Jul 20	24.7
06226	2005 Feb 19	23.6	17522	2017 Apr 08	49.4
06228	2005 Feb 25	15.8	17523	2016 Aug 31	49.4
06229	2005 Feb 23	22.6	17524	2015 Sep 08	22.8
06250	2005 Feb 21	7.0	17525	2017 Apr 22	24.5
06252	2005 Sep 07	29.7	17526	2015 Sep 20	49.4
17133	2016 Jun 18	30.2	17527	2015 Oct 11	26.3
17134	2017 May 20	28.5	17528	2015 Aug 30	49.1
17135	2017 Jan 20	19.8	17529	2016 Dec 15	34.9
17136	2017 Jan 26	22.2	17530	2015 Apr 19	21.1
17137	2017 Mar 29	25.0	17650	2015 Apr 22	28.2
17138	2016 Jul 25	26.0	17710	2015 Aug 07	19.8
17139	2016 Sep 16	39.5	18441	2015 Sep 14	24.6
17140	2016 Oct 02	34.2	18641	2015 Oct 15	22.4
17141	2015 Aug 01	29.7	18682	2015 Oct 14	22.6
17142	2017 Apr 20	23.3	18683	2015 Oct 18	15.6
17143	2015 Sep 03	26.9	18688	2015 Nov 01	34.4
17144	2015 May 03	49.4	18871	2016 Jun 13	21.6
17507	2016 Nov 12	32.6	18886	2016 Jul 23	22.2
17508	2015 Oct 28	14.9	19888	2016 Oct 01	19.5
17509	2016 Jul 10	51.4	19956	2016 Dec 10	54.3
17510	2016 Jun 26	37.1	19989	2017 Feb 12	41.5
17511	2017 May 10	15.9	19996	2017 Jan 28	28.1
17512	2016 Sep 15	66.9	20043	2017 Mar 25	29.6
17513	2016 Aug 15	49.4	20044	2017 Mar 26	14.9
17514	2016 Dec 13	49.4	20048	2017 May 19	22.6
17515	2017 Mar 21	39.3	20077	2017 May 13	27.7
17516	2016 Aug 18	49.0	20079	2017 May 21	23.8
				Total Exposure Time	1958.7

Note.
[a] Net exposure after background flare removal.

In order to correct for small astrometric errors, ObsID 05831 was chosen as a reference for its high total count. A raw 0.5–7.0 keV image was made in a rectangular region of $160'' \times 120''$ centered on Cyg A. For each remaining ObsID, the events were reprojected onto the sky to match ObsID 05831, and a raw 0.5–7.0 keV image was made for the same region. The cross-correlation between each raw image and the ObsID 05831 image was then fitted with a Lorentzian profile to determine the offset between them. The astrometric translation required to align each data set with ObsID 05831 was then applied to the event list using the wcs_update CIAO routine. The root mean square translation for the images was $\Delta x_{\rm rms} = 0\farcs82$ and $\Delta y_{\rm rms} = 0\farcs25$. This approach produced notably sharper features in a co-added image of Cyg A than those using the CIAO tools designed to coalign the point sources.

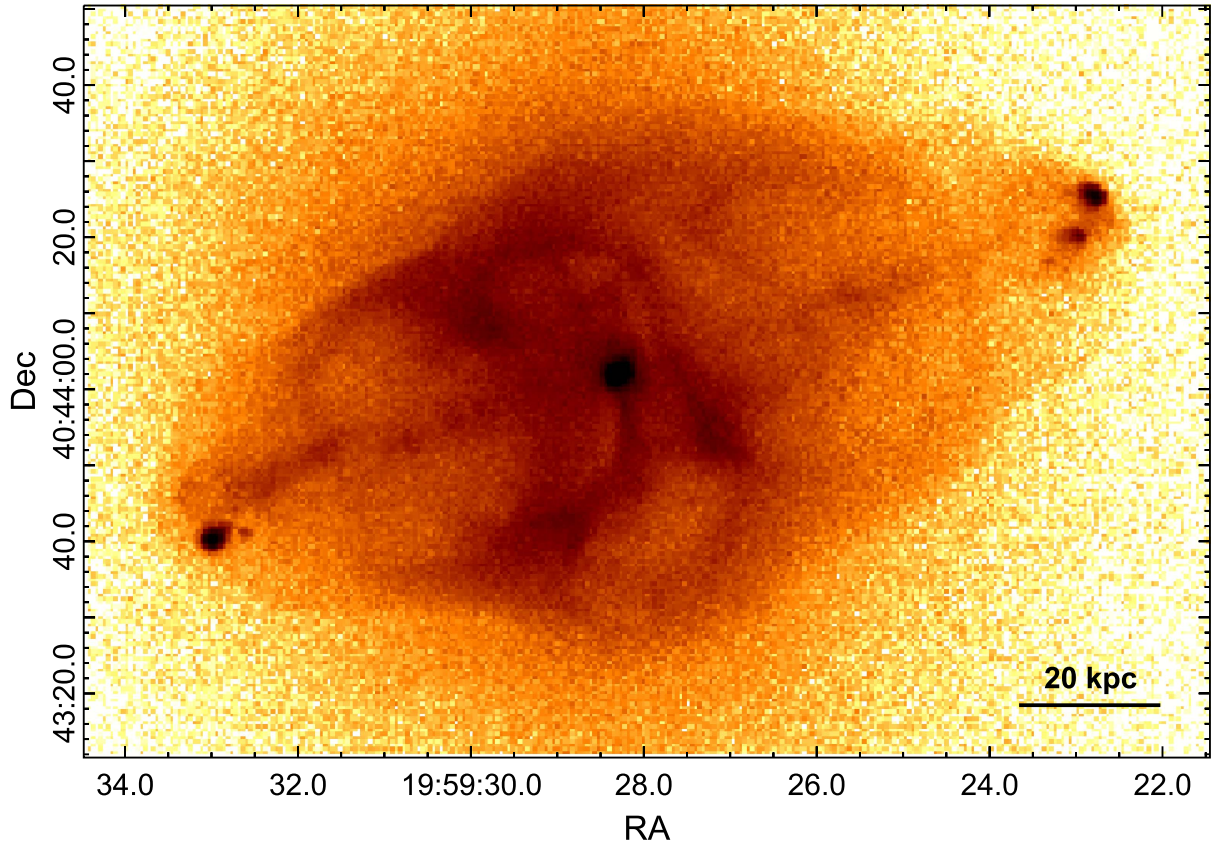

Figure 1. 0.5–7.0 keV *Chandra* image of Cygnus A. The image has been background-subtracted and exposure-corrected and is made using the *Chandra* observations listed in Table 1.

The appropriate blank-sky exposures from CALDB were processed in an analogous fashion to the data to simulate a background event file for each observation. The background rates were scaled to match observed rates in the 10–12 keV energy band. Exposure maps for the 0.5–7.0 keV energy band were created assuming the spectral model PHABS × APEC, with a temperature $kT = 5.5$ keV and an abundance $Z = 0.66$ relative to the solar abundances of Anders & Grevesse (1989). A 0.5–7.0 keV, background-subtracted, exposure-corrected image made from the combined exposures is shown in Figure 1. The cocoon shock is clearly seen enveloping the eastern and western hotspots and the other complex structure that surrounds the central AGN (Figure 2).

All spectra used in the following analysis were binned to have a minimum of 1 count per bin and are fitted over the energy range 0.5–7.0 keV using the Cash statistic (cstat) in XSPEC v12.9.1h (Arnaud 1996). Abundances are scaled to the solar abundances of Anders & Grevesse (1989).

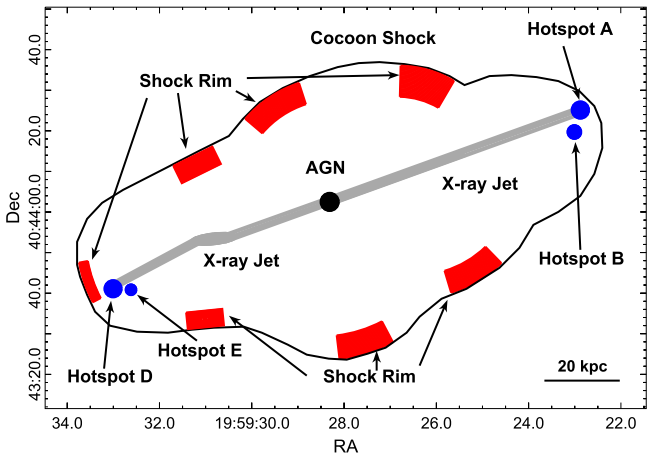

Figure 2. Schematic image of Cygnus A with key features (AGN, cocoon shock, hotspots, jets) labeled for ease of visibility. Several inner rims of the shock front that are visible in the original image are also highlighted.

3. Properties of the Unshocked ICM

Deprojections were used to determine the properties of the unshocked ICM in the vicinity of the cocoon shock. The region around Cyg A was divided, along the jets and a perpendicular axis, into quadrants about the AGN, as shown in Figure 3. A region around the central AGN and circular regions over the lobes and hotspots were masked. Annular sectors were then defined in each quadrant, out to a radius of 300″, to have a minimum of 25,000 counts in each. Annular sectors were also defined to cover quadrants 2–4, containing a minimum of 75,000 counts per region. The northwest sector (quadrant 1) was excluded, as it is most affected by the merger shock associated with the infalling subcluster (Ledlow et al. 2005; M. W. Wise et al. 2018, in preparation)

For the deprojections, each set of annular spectra was fitted simultaneously using the XSPEC model PROJCT × PHABS × MEKAL. Two additional thermal components are included as a second model. The first of these allows for emission from the cluster atmosphere beyond the deprojection region, under the assumption that the gas there is distributed as an isothermal beta model (Nulsen et al. 2010). The beta parameter for this model was determined by fitting the surface brightness profile

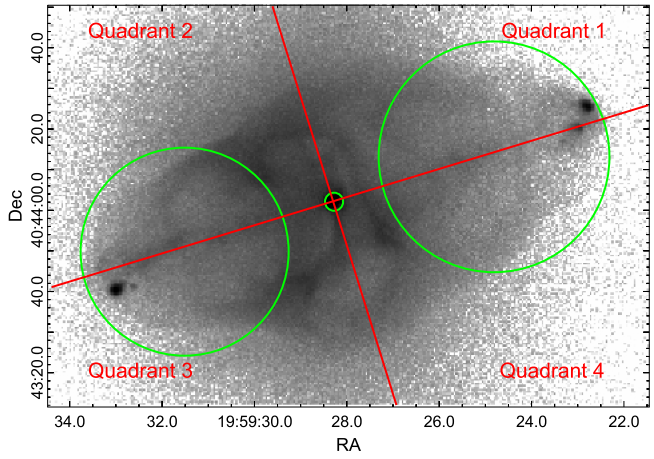

Figure 3. Regions used for deprojections. The red lines show the boundaries of the four quadrants. Green circles show the regions excluded. Data for each quadrant were analyzed separately, and quadrants 2–4 were also deprojected together. Quadrant 1 is excluded from the latter group, since it is most affected by the infalling subcluster.

from 200″ to 300″ in each quadrant. The second component of the additional model represents soft thermal emission of uniform surface brightness, to allow for foreground emission from our Galaxy. The deprojection provides temperatures and abundances directly, while values of the electron densities, n_e, are determined from the norms of the thermal models determined with PROJCT, assuming that the density is uniform in the spherical shells. Total gas pressures are determined as $n_{tot}kT$, where the total particle number density is $n_{tot} \simeq 1.93n_e$.

The deprojection results are plotted in Figure 4, and the corresponding data tables are provided in the supplemental materials. Average values are in excellent agreement with the deprojection results of Smith et al. (2002). The radius of the cocoon shock varies between and within the sectors, in the range indicated by the gray band in Figure 4. Within the shock, the deprojection results must be treated with caution due to the evident departures from spherical symmetry, which is discussed in more detail by Duffy et al. (2018). Beyond it, the electron density profiles are remarkably consistent from quadrant to quadrant, only showing modest departures from spherical symmetry. The largest discrepancy occurs at ≃80″ in the northwest quadrant (quadrant 1), where the density is roughly 30% lower than in the other quadrants and the temperature is markedly higher. There is more scatter between the temperatures in the different quadrants, which are significantly higher at larger radii in the northern sectors and lowest to the southeast, on the opposite side to the infalling subcluster. At a radius of 200″, the pressures span a range of ≃2 from northwest to southeast, which reduces substantially at smaller radii, outside the shock. The temperature profiles each show a modest local peak at about the shock radius. The abundance errors largely obscure any structure, apart from an overall decline with radius.

4. Cocoon Shock Strength

In this section, we determine the shock strength at several locations on the cocoon shock by fitting its surface brightness profile. Temperature jumps and shock compression are considered for consistency checks. Later, in Section 5, we also examine the pressure jump in each sector, comparing it to a direct estimate of the gas pressure within the cocoon.

To measure the surface brightness profiles of the cocoon shock, a number of segments of the shock front were chosen where the shock is clearly visible and continuous. A sector was defined to enclose each segment such that an arc in the sector best matches the front. This procedure gave the nine sectors marked in Figure 5. A surface brightness profile of the shock was extracted for each sector. To model the surface brightness profile of a shock front, its radius of curvature relative to our line of sight is critical, as that determines how much of the line of sight lies within the shocked gas at any projected distance from the front. In practice, the radius of curvature is determined by the coordinate used in the surface brightness profile. The zero point of this coordinate therefore needs to be chosen suitably. Under the assumption that the cocoon shock is axially symmetric about the X-ray jet, the center of the jet is chosen as the center of every sector. The units of the radial coordinate do not affect the estimated shock strength, so there is no need to correct for the inclination between each sector and the axis of the cocoon.

The models for the surface brightness profile assume that the emission arises from hot gas. All profiles were therefore truncated prior to entering cavities and/or regions of nonthermal emission within the shock. At larger radii, the profiles were truncated before any noticeable departure from a constant power-law slope. Each sector was also selected to avoid evident structure, such as the region directly to the south of the AGN where the gas rim appears narrowest. Limiting the transverse extent of a sector reduces the signal-to-noise ratio of the surface brightness profile, while limiting the radial extent of the fit generally increases the uncertainty in the fitted parameters. Nevertheless, the parameters are well-determined in all the regions selected. The limits of each sector are shown, together with an arc marking the fitted shock, in Figure 5.

4.1. Broken Power-law Fits to Surface Brightness Profiles

The broken power-law model for the surface brightness profile is obtained by assuming that the distribution of volume emissivity is spherical in three dimensions, with the form

$$\varepsilon(r) = \begin{cases} A_1 (r/r_s)^{-\eta_1}, & \text{for } r < r_s, \\ A_2 (r/r_s)^{-\eta_2}, & \text{for } r > r_s, \end{cases} \quad (1)$$

and the constant parameters A_1, A_2, η_1, η_2, and r_s, where r_s is the shock radius. Projecting the volume emissivity onto the sky (by integrating along the line of sight) gives the model surface brightness profile, which is binned and fitted to the observed profile to determine the parameters. For thermal plasma, the power radiated per unit volume is $n_e n_H \Lambda(T, Z)$, where the cooling function Λ depends on the temperature T and composition Z of the gas. The composition is expected to vary slowly near the shock and the *Chandra* broadband response for thermal plasma depends very weakly on the temperature in the range of interest, so the brightness is almost independent of the temperature. Since the proton number density, n_H, is a constant multiple of the electron number density, we can therefore estimate the density jump at the shock as $\sqrt{A_1/A_2}$. The shock Mach number is then determined from the density jump using the Rankine–Hugoniot jump conditions for gas with the ratio of specific heats, $\Gamma = 5/3$. The density jumps and Mach numbers obtained from the broken power-law model are given for the nine sectors in columns 3 and 4 of Table 2.

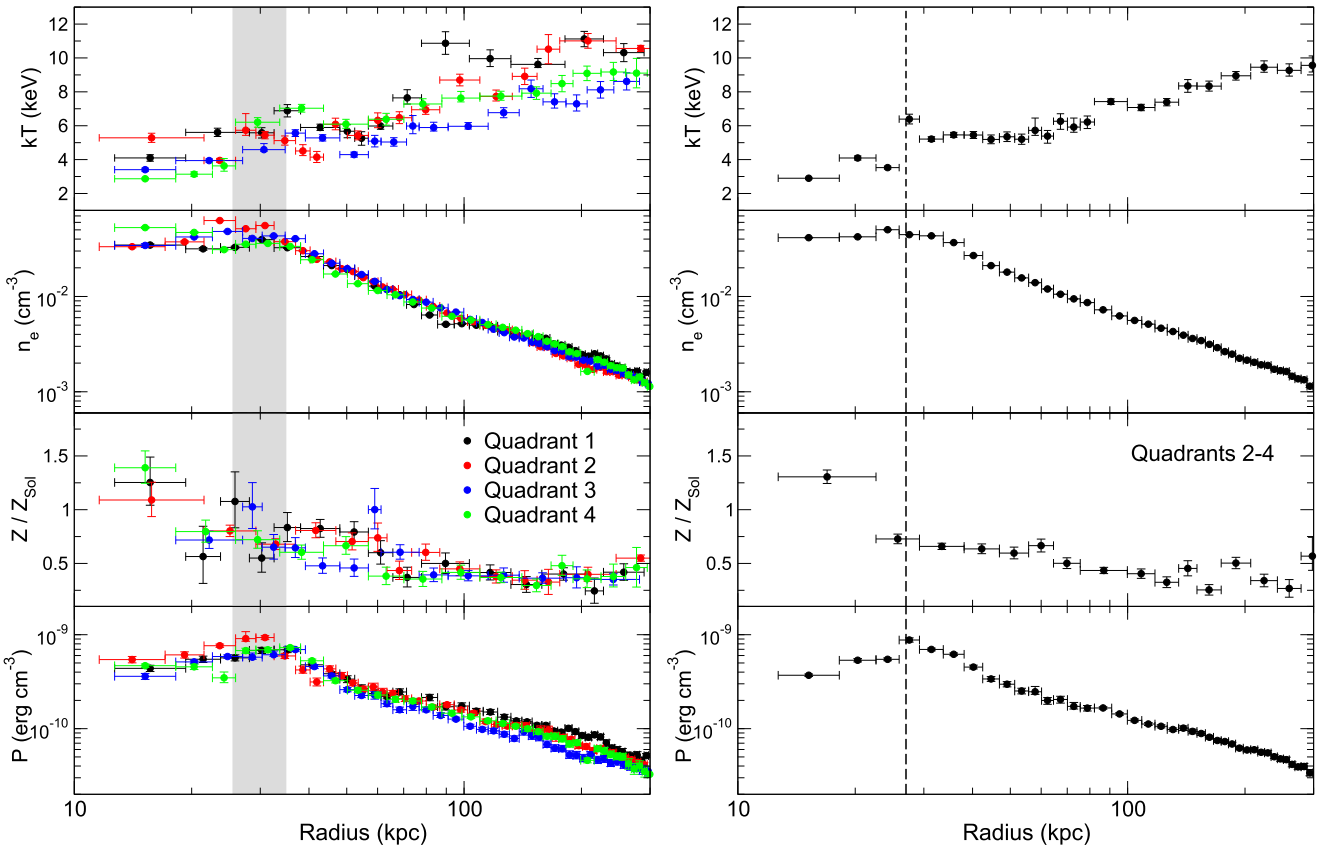

Figure 4. Deprojected profiles of the temperature, electron density, abundance, and pressure for the four quadrants marked in Figure 3 (left) and for quadrants 2–4 combined (right). The gray stripe indicates the range of shock radii, while the dashed line shows the average shock radius. The data used to create this figure are available.

4.2. Hydrodynamic Shock Model

The surface brightness profiles were also fitted using the spherical hydrodynamic model described in Nulsen et al. (2005). In this model, the unshocked gas is assumed to be isothermal and hydrostatic, with a power-law density distribution, $\rho(r) \propto r^{-\eta}$. A shock is launched by an initial, explosive energy release at the center of the grid and the subsequent gas flow is calculated using a spherically symmetric hydrodynamic code. The preshock temperature is chosen to match the temperature of the gas just outside the shock. Note that, for this model, the *Chandra* response is included in computing the surface brightness profiles to fit to the data. Since the model is scale-free, it can be rescaled at each time step to obtain the best fit to the surface brightness profile. Optimizing the fit over time for one simulation gives a best-fitting shock radius and Mach number. Simulations are then run for a range of initial density power laws, η, to find the global best fit.

Although this model still represents a highly simplified version of the cocoon shock in Cyg A, it provides a better account than the broken power-law model of the rapid expansion of the shocked gas that occurs immediately after the shock. As a more physically accurate model, we therefore prefer its results to those for the broken power-law model. However, the broken power-law model has been used widely, so it is interesting to compare the results. Density jumps and Mach numbers for the hydrodynamic model are given in columns 5 and 6 of Table 2 and an example fit for region 1 is shown in Figure 5. Although the differences are marginal in most cases, the shock strengths for the hydrodynamic model are systematically higher than those for the broken power-law model, except for region 1. Given the greater fidelity of the hydrodynamic model, the results indicate that the broken power-law fits tend to systematically underestimate the shock strength, although by a small amount for these relatively weak shocks. Results from the hydrodynamic model are used in the remainder of this article.

4.3. Shock Temperature Jumps

Two spectra were extracted from each of the nine sectors shown in Figure 5, from the regions inside and outside the fitted shock radius. Temperatures were determined by fitting the pre- and postshock spectra with the single-temperature model PHABS × APEC in XSPEC. Abundances were assumed to be the same on either side of the shock in each sector, as we do not expect large local variations. Temperatures and normalizations were allowed to vary independently. Since emission from the unshocked gas is projected onto the region inside the shock, a two-temperature model was also tried for the region within the shock, with the temperature of the one thermal component tied to that of the region outside the shock. However, this model did not significantly improve the fits. The abundances and fitted temperatures for each sector are given in Table 2, with values from within the shock denoted $kT_{\rm in}$ and those from outside denoted $kT_{\rm out}$.

For $\Gamma = 5/3$, the temperature jump in a weak shock is numerically close to the value of its Mach number (for

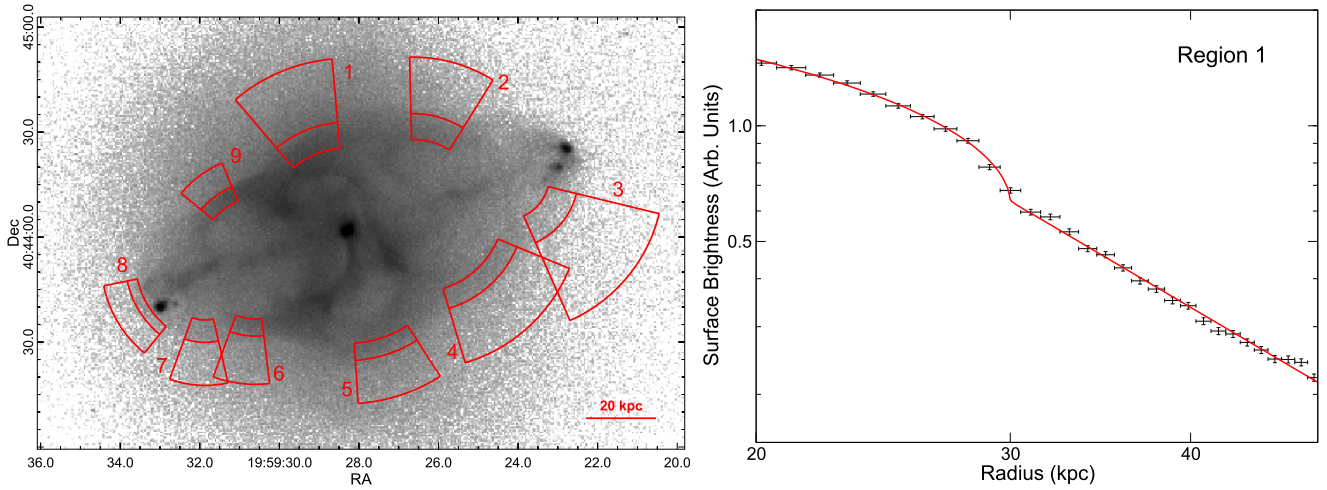

Figure 5. Left: sectors used to measure the surface brightness profiles of the cocoon shock. Inner and outer arcs mark the range of the radius fitted, and the middle arc marks the best-fit radius of the density discontinuity. Right: surface brightness profile and best-fit hydrodynamic model for sector 1 (Section 4.2).

$M = 1.18$, the temperature jump is 1.17, while for $M = 1.66$, it is 1.67), so the Mach numbers from Table 2 should be directly comparable to the temperature ratios in its last column. However, several factors reduce the jumps in the projected temperature. First, unshocked gas projected onto the postshock region is generally cooler than the shocked gas, which lowers the fitted postshock temperatures. Second, adiabatic expansion causes a rapid decrease in the gas temperature behind the shock, so that the finite width of the postshock spectral regions inevitably makes their mean temperatures lower than the immediate postshock temperatures. Third, from the deprojected temperature profiles (Figure 4), the shock appears to be propagating up a preexisting temperature gradient, which would now make the gas in the preshock region hotter than the gas in the postshock region was before being shocked. All three effects tend to make the jump measured in the projected temperature lower than the jump at the shock front. Thus, the measured temperature ratios should be regarded as lower limits on the actual shock temperature jumps. Although the measured jumps do not provide good quantitative measures of the shock strength, taken together, they make a strong case that the temperature increases in the shock. Furthermore, for the Mach numbers determined from the surface brightness profiles, the measured ratios in the projected temperature are broadly consistent with the expectations of numerical models (e.g., Forman et al. 2007). In particular, the temperature jumps are higher in the sectors with higher Mach numbers.

4.4. Shock Compression

Within the cocoon shock, there is a clear anticorrelation between the X-ray emission and the 5 GHz radio emission, as shown in Figure 6. This and the detailed matches between radio and X-ray features around the edges of the lobes make a strong case that the radio plasma has displaced the X-ray-emitting gas, as found in many less powerful radio galaxies (e.g., McNamara & Nulsen 2007; M. W. Wise et al. 2018, in preparation). The compression of the gas into narrow rims around the radio lobes is clearest in the eastern lobe, between regions 6 and 9 of Figure 5. This is also seen in the surface brightness cut through the cocoon in this region, plotted in red in Figure 7.

Here we ask whether the compression is consistent with the estimated shock strengths for regions 6 and 9. To estimate how much the displaced gas has been compressed, we first assume that all of the gas initially within the lobe remains in the rims (rather than being displaced toward the cluster center, for example). We also assume cylindrical symmetry about the axis of the X-ray jet. For a fixed amount of gas, the mean density is inversely proportional to the volume, so that the compression is given by V_i/V_f, where V_i and V_f are the initial and final volumes occupied by the gas. If the gas was displaced perpendicular to the jet axis, we would have $V_i/V_f = r_o^2/(r_o^2 - r_i^2)$ (cylindrical motion), where r_i and r_o are the inner and outer radii of the compressed shell. More generally, as the gas is pushed away from the jet axis, fluid elements will also separate in the direction along the axis. If the separation increases linearly with distance from the axis, the volume would scale as $r^2 + \beta r^3$, for some constant $\beta \geqslant 0$. In the limit $\beta r \gg 1$, we would then have $V_i/V_f = r_o^3/(r_o^3 - r_i^3)$, corresponding to spherical motion (note that $\beta r \ll 1$ gives the cylindrical case).

For region 6, we estimate that the perpendicular distance from the jet axis to the inner edge of the compressed rim is $r_i = 17\farcs6$ and to the shock front it is $r_o = 24\farcs6$, giving compressions ranging from 1.58 to 2.05 for the spherical and cylindrical cases, respectively. From the Rankine–Hugoniot jump conditions, for Mach number of 1.47, the shock compression would be a factor of 1.67, which lies in this range. For region 9, we find $r_i = 16\farcs4$ and $r_o = 22\farcs1$, giving compressions in the range 1.69–2.23. For a Mach number of 1.66, the shock compression is a factor of 1.92, which is also within the estimated range. We note that these results are rough, and other issues, such as the rapid expansion of the gas behind the shock and likely variation of the shock strength over time, add systematic uncertainty. Despite these concerns, it is reassuring that the Mach numbers determined from the surface brightness profiles are consistent with our estimates of the compression of the gas in the rims.

4.5. Diffuse Lobe Emission

Consider a cylindrical shell of uniform X-ray emission, between the inner and outer radii a and b, respectively. Projecting onto the sky (in any direction but parallel to the axis of the cylinder), the surface brightness on a line of sight that passes within a distance $\varpi < a$ of its axis will be proportional to $\sqrt{b^2 - \varpi^2} - \sqrt{a^2 - \varpi^2}$, which is an increasing function of

Table 2
Shock Parameters

Region[a]	Discontinuity Distance[b] (kpc)	Broken Power Law		1D Hydro Model		Abundance[c]	$kT_{\rm out}$ (keV)	$kT_{\rm in}$ (keV)	$kT_{\rm in}/kT_{\rm out}$
		Density Jump	Mach Number	Density Jump	Mach Number				
1	32.9 ± 0.2	$1.31^{+0.02}_{-0.02}$	$1.21^{+0.01}_{-0.01}$	$1.27^{+0.01}_{-0.01}$	$1.18^{+0.01}_{-0.01}$	$0.60^{+0.03}_{-0.03}$	$5.16^{+0.06}_{-0.06}$	$5.26^{+0.05}_{-0.05}$	$1.02^{+0.02}_{-0.02}$
2	46.1 ± 0.7	$1.52^{+0.03}_{-0.01}$	$1.35^{+0.01}_{-0.02}$	$1.58^{+0.03}_{-0.01}$	$1.40^{+0.02}_{-0.01}$	$0.65^{+0.06}_{-0.06}$	$7.87^{+0.24}_{-0.24}$	$7.47^{+0.22}_{-0.21}$	$0.95^{+0.06}_{-0.05}$
3	68.3 ± 0.4	$1.55^{+0.11}_{-0.07}$	$1.38^{+0.08}_{-0.05}$	$1.79^{+0.12}_{-0.03}$	$1.56^{+0.10}_{-0.03}$	$0.52^{+0.08}_{-0.07}$	$9.09^{+0.44}_{-0.44}$	$8.95^{+0.49}_{-0.40}$	$0.98^{+0.11}_{-0.08}$
4	48.7 ± 0.4	$1.56^{+0.04}_{-0.04}$	$1.38^{+0.04}_{-0.03}$	$1.66^{+0.03}_{-0.03}$	$1.46^{+0.02}_{-0.02}$	$0.44^{+0.04}_{-0.04}$	$7.54^{+0.18}_{-0.18}$	$8.08^{+0.23}_{-0.22}$	$1.07^{+0.06}_{-0.05}$
5	41.0 ± 0.3	$1.31^{+0.04}_{-0.05}$	$1.21^{+0.03}_{-0.03}$	$1.43^{+0.03}_{-0.03}$	$1.29^{+0.02}_{-0.02}$	$0.44^{+0.03}_{-0.04}$	$5.74^{+0.13}_{-0.13}$	$6.05^{+0.17}_{-0.16}$	$1.05^{+0.04}_{-0.05}$
6	45.6 ± 0.3	$1.58^{+0.06}_{-0.05}$	$1.40^{+0.04}_{-0.03}$	$1.67^{+0.04}_{-0.04}$	$1.47^{+0.03}_{-0.03}$	$0.68^{+0.05}_{-0.05}$	$5.31^{+0.10}_{-0.10}$	$6.98^{+0.28}_{-0.25}$	$1.31^{+0.09}_{-0.07}$
7	57.3 ± 0.2	$1.72^{+0.22}_{-0.15}$	$1.51^{+0.15}_{-0.11}$	$1.82^{+0.09}_{-0.08}$	$1.58^{+0.07}_{-0.06}$	$0.61^{+0.06}_{-0.06}$	$5.82^{+0.18}_{-0.18}$	$7.66^{+0.41}_{-0.40}$	$1.32^{+0.11}_{-0.11}$
8	70.7 ± 0.5	$1.82^{+0.38}_{-0.23}$	$1.58^{+0.33}_{-0.18}$	$1.87^{+0.14}_{-0.17}$	$1.62^{+0.12}_{-0.13}$	$0.49^{+0.08}_{-0.07}$	$6.29^{+0.24}_{-0.23}$	$7.05^{+0.43}_{-0.35}$	$1.12^{+0.11}_{-0.09}$
9	43.0 ± 0.2	$1.90^{+0.10}_{-0.09}$	$1.65^{+0.06}_{-0.06}$	$1.92^{+0.07}_{-0.07}$	$1.66^{+0.06}_{-0.06}$	$0.65^{+0.06}_{-0.06}$	$5.51^{+0.17}_{-0.14}$	$6.99^{+0.30}_{-0.20}$	$1.27^{+0.09}_{-0.07}$

Notes.
[a] Region number from Figure 5.
[b] Average projected distance from the AGN to the shock front.
[c] Relative to the scale of Anders & Grevesse (1989).

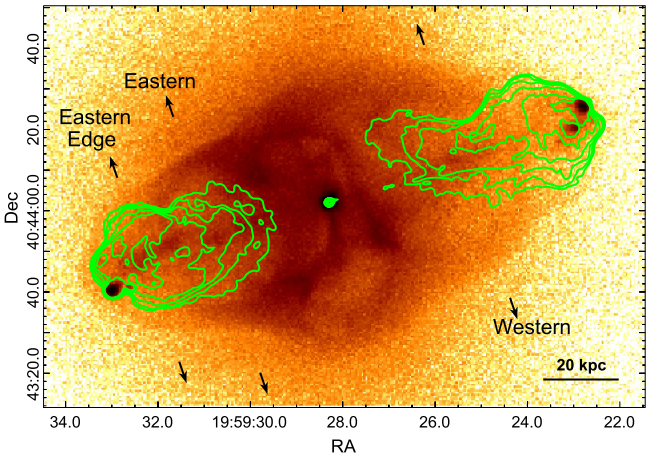

Figure 6. 0.5–7.0 keV *Chandra* image of Cygnus A with 5 GHz VLA (green) contours overlaid. The contours start at 3σ and are spaced by a factor of two. Radio emission fills the eastern and western cavities, and the central radio peak is coincident with the AGN. Arrows indicate the positions of the surface brightness cuts through the cocoon discussed in Sections 4.4 and 4.5.

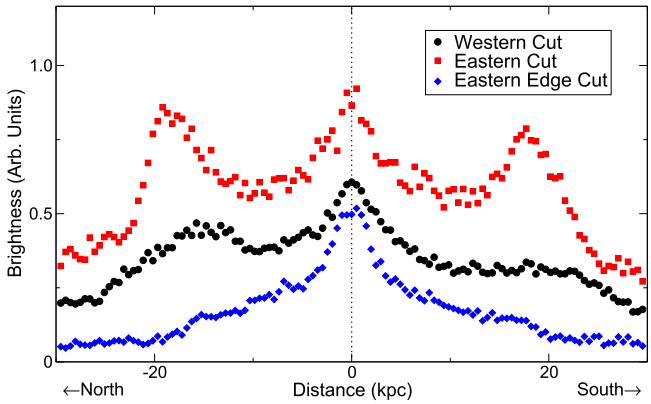

Figure 7. Surface brightness cuts perpendicular to the radio axis. The positions of the three cuts are indicated by arrows in Figure 5. Each cut through the radio cocoon is centered on the peak over the X-ray jet. The bright rims of compressed gas bounding the X-ray "cavity" on the north and south are clearest for the eastern cut (red). Further to the east (blue), there appear to be no bright rims, and the surface brightness rises monotonically toward the center of the jet, requiring diffuse X-ray emission from throughout the lobe. To the west, the northern rim is less distinct and no rim is evident to the south.

ϖ. Decomposing any cylindrically symmetric distribution of X-ray emission into thin cylindrical shells of uniform emission, this shows that if there is a hollow central region, the surface brightness will always increase with distance away from the symmetry axis inside the hollow region. Although the issue is more complex for a more general axisymmetric distribution of X-ray emission, it generally remains true that the surface brightness must increase with distance from the symmetry axis if the central region is hollow.

This is the basis of the discussion in Section 4.4 above. Particularly in the inner eastern part of the cocoon, we see clear evidence that the radio plasma has displaced the hot ICM, compressing it into a dense shell between the radio lobe and the cocoon shock. This is manifested in the surface brightness cut (red points in Figure 7) as sharp decreases in the surface brightness inside the northern and southern rims. Emission from the central "X-ray jet" partly fills in the X-ray cavity, but the decrease in X-ray surface brightness within the rims shows that any X-ray emission from inside the cavity must be considerably fainter than that from within the rims.

Farther toward the eastern hotspots, although the shock front remains quite visible in the X-ray image, the compressed shell of shocked gas is no longer readily discernible. This is confirmed by the "eastern edge" surface brightness cut in Figure 7 (blue points), which shows that the X-ray emission rises inwards, all the way to the central peak over the X-ray jet. Such a surface brightness profile is inconsistent with a hollow shell of X-ray emission. It requires that there is diffuse X-ray emission throughout the lobe region, peaking toward the jet axis. Almost certainly, the centrally peaked X-ray emission from within the bright radio lobe is the synchrotron self-Comptom emission reported previously (Hardcastle & Croston 2010; Yaji et al. 2010; de Vries et al. 2018). Given that the shock is likely to be stronger here than in regions closer to the AGN (due to higher lobe pressure in the vicinity of the hotspots and to lower external pressure), we should expect the shell of the shock-compressed gas to be thinner relative to the size of the cavity than it is in regions closer to the AGN. There must be some thermal emission from the shocked gas, but it is hard to

Table 3
A Comparison of Shock Pressures

Region	Pressure (10^{-10} erg cm^{-3})	
	Postshock[a]	Rim[b]
1	$9.59^{+0.83}_{-0.80}$	$8.44^{+0.21}_{-0.21}$
2	$8.46^{+0.69}_{-0.66}$	$8.34^{+0.39}_{-0.38}$
3	$5.74^{+0.93}_{-0.85}$	$7.12^{+0.60}_{-0.55}$
4	$7.83^{+0.70}_{-0.67}$	$8.48^{+0.58}_{-0.40}$
5	$9.02^{+0.75}_{-0.72}$	$9.07^{+0.45}_{-0.43}$
6	$8.93^{+0.88}_{-0.83}$	$10.77^{+0.73}_{-0.65}$
7	$6.51^{+1.19}_{-1.08}$	$9.59^{+0.50}_{-0.49}$
8	$5.57^{+1.37}_{-1.18}$	$6.17^{+0.65}_{-0.58}$
9	$10.04^{+1.88}_{-1.69}$	$12.16^{+0.91}_{-0.73}$

Notes.
[a] Determined from preshock and shock strength, Section 5.1.
[b] Determined from XSPEC norms of spectra, Section 5.2.

distinguish from nonthermal emission from within the lobe. As a result, it is difficult to know where the thermal shock model is applicable and, therefore, to determine the shock strength. For this reason, the regions used to measure the shock profiles (Figure 5) lie outside the radio lobes, although this was not possible for region 3.

5. Cocoon Pressure

In this section, we consider estimates of the pressure within the radio cocoon, which is a key parameter of physical models for the lobes. Jet momentum can maintain higher pressures in the hotspots, driving supersonic flows and nonuniform pressures in small surrounding regions (e.g., Mathews & Guo 2012). However, the sound speed is expected to be very high in the plasma filling the radio lobes, so that the pressure should be relatively uniform away from the vicinity of the hotspots. The pressure is also expected to be fairly uniform within the rim of compressed gas between the radio lobes and the cocoon shock, so that the pressure in the rim can provide a good measure of the pressure in the adjacent lobe.

5.1. Postshock Pressure

Our first determination of the pressures in the lobes relies on the shock fits. For each of the regions marked in Figure 5, the deprojected pressure profiles of Section 3 can be used to estimate a preshock pressure. The deprojected distance from a shock to the AGN is determined from the projected shock radius in Table 2, assuming that the cocoon axis is inclined at 55° to the line of sight (Vestergaard & Barthel 1993). Thus, the displacement from the AGN parallel to the jet axis is boosted by a factor of $1/\sin 55°$, while the displacement perpendicular to the axis is unaltered. The preshock pressure is taken from the deprojected pressure profile for the appropriate quadrant at the deprojected distance from the AGN. For the sectors that cross between two quadrants (regions 1, 5, and 8), the pressure values are averaged for those quadrants. The Mach number for the hydrodynamic model (Table 2) is then used to calculate the pressure jump in the shock, hence the postshock pressure. The resulting postshock pressures are listed in the second column of Table 3, and their range is modest. If they are consistent with a single value, $p_{\rm ps}$, the residual

$$\chi^2_{\rm ps} = \sum_i \left(\frac{p_i - p_{\rm ps}}{\sigma_i} \right)^2 \quad (2)$$

should have an approximately chi-squared distribution. It is minimized by setting $p_{\rm ps}$ to the weighted mean,

$$p_{\rm ps} = \frac{\sum_i p_i/\sigma_i^2}{\sum_i 1/\sigma_i^2}. \quad (3)$$

Using this value in the residual reduces the number of degrees of freedom by one. Excluding the outlying values for regions 3 and 8 and taking σ_i to be the average of the upper and lower sigmas for each measurement, the weighted mean postshock pressure is $p_{\rm ps} = 8.56 \pm 0.31 \times 10^{-10}$ erg cm^{-3}, giving the residual $\chi^2_{\rm ps} = 7.28$, near the 70% upper confidence limit for a chi-squared distribution with six degrees of freedom. Thus, the postshock pressures do not show evidence for pressure variations within the cocoon.

Several sources of systematic error inherent to our model affect the postshock pressures. First, the geometry of the system is fixed by assuming axial symmetry about the center of the X-ray jet. This fixes the shape of the front and the spatial distribution of the gas, which determine a surface brightness profile. Although theory and the appearance of Cyg A support the assumption of axial symmetry, it is clearly approximate. In particular, local irregularities on the front can be caused by gas flows within the ICM, stochastic precession of the jet, or variations in jet power (Heinz et al. 2006; Mendygral et al. 2012). Small-scale irregularities have the effect of smoothing the projected surface brightness profile, making the shock appear weaker (Nulsen et al. 2013). Larger-scale asymmetries can alter the curvature of the projected front. The impact of such effects is expected to be greater on the outer parts of the front (regions 3, 7 and 8), where the scale of the intrinsic curvature is smaller, causing the front seen in projection to appear less clearly defined. They may well account for the anomalous postshock pressures of region 3 and 8.

A second related source of systematic error is the implicit assumption that the densest unshocked gas on our line of sight coincides with the projected shock front. This maximizes the density of the gas being shocked, hence the contrast in surface brightness at the shock. If it is incorrect, our surface brightness fits underestimate the true shock strength. The asymmetry of the X-ray image and the evidence that the AGN is moving through the ICM (Section 6.2) both make it unlikely that this assumption is completely accurate.

A third source of systematic error for the postshock pressures is the poorly constrained inclination angle of the jet axis. Various inclination angles have been used in prior Cyg A analyses, ranging from 35°–80° (Bartel et al. 1995; Boccardi et al. 2016). Recalculating the postshock pressures using the minimum and maximum angles of this range produced a ∼20% decrease and increase in the average postshock pressure, respectively. The estimates of rim pressures in the next section rely on fewer assumptions, providing some check on these sources of systematic error.

5.2. Rim Pressure

The rims of the eastern cavity, in particular, are significantly brighter than the adjacent unshocked gas. This suggests that the temperature and density in a rim can be estimated simply by ignoring the emission of the unshocked gas projected onto the rim. Doing so overestimates the gas density in the rim, hence also its pressure. A more accurate result might be obtained by deprojection, where we estimate how much emission from adjacent regions is projected onto the rim and, in effect, treat it as a background contribution to the rim spectrum. However, the results of deprojection are sensitive to unavoidable assumptions about the distribution of the unshocked gas. Rather than attempting to model the distribution of unshocked gas, we can simply treat the adjacent region as a local background, almost certainly overestimating the amount of emission projected onto the rim. The upshot will be to underestimate the pressure in the rim. Combining these two estimates provides lower and upper bounds on the pressure in the rim, which can bracket its pressure tightly when the rim is much brighter than the adjacent, unshocked region.

We apply this approach to the spectra that were used to determine the pre- and postshock temperatures in Section 4.3. Each sector in Figure 5 is divided at the shock radius, and two spectra are extracted. The spectrum of the inner region represents emission from the compressed rim, and it is used to determine gas properties in the rim by fitting the absorbed thermal model, PHABS × APEC, in XSPEC. Using a blank-sky background, the fit gives us an upper limit on the pressure, while using the preshock spectrum for background gives a lower limit. Treating the gas in the rim as uniform, its density can be determined in cgs units from the XSPEC norm,

$$\mathrm{NORM} = \frac{10^{-14} n_{\mathrm{e}} n_{\mathrm{H}} V}{4\pi [D_{\mathrm{A}}(1+z)]^2}, \tag{4}$$

where D_{A} is the angular diameter distance, z is the redshift, and V is the volume of the emitting region, and the proton number density is $n_{\mathrm{H}} = 0.86 n_{\mathrm{e}}$. To estimate the emitting volume, we assume again that the rim is symmetric under rotation about the jet axis. For a spectrum extracted from an annular sector, the emitting volume then lies in the intersection between a spherical shell and a cylindrical shell extending to infinity along our line of sight, with the same inner and outer radii, restricted to the angular range of the sector, $\delta\phi$. The volume of the region is therefore

$$V = \frac{2\delta\phi}{3}(r_{\mathrm{o}}^2 - r_{\mathrm{i}}^2)^{3/2}, \tag{5}$$

where r_{i} and r_{o} are the inner and outer radii of the rim. As in Section 3, the rim pressure is $n_{\mathrm{tot}} kT$, with $n_{\mathrm{tot}} = 1.93 n_{\mathrm{e}}$, and the temperature determined from the spectral fit. The right-hand column of Table 3 gives the average of the upper and lower limits on the pressures, with systematic errors equal to half the difference between the limits combined in quadrature with the lower and upper confidence ranges.

Omitting the outlying value for region 8, the weighted mean of the rim pressures is (Equation (3)) $p_{\mathrm{rim}} = 8.72 \pm 0.14 \times 10^{-10}$ erg cm^{-3}, in agreement with the mean postshock pressure (Section 5.1). However, using this value to compute the residual (Equation (2)) gives $\chi^2_{\mathrm{rim}} = 40.88$ for seven degrees of freedom, exceeding the 99% confidence level and indicating that the pressure does vary significantly around the rim. From Table 3, the pressures are higher in the eastern lobe. The weighted mean of the rim pressures for the eastern regions (6, 7 and 9) is $10.41 \pm 0.36 \times 10^{-10}$ erg cm^{-3}, while that for the central and western regions (1, 2, 3, 4 and 5) is $8.41 \pm 0.15 \times 10^{-10}$ erg cm^{-3}, differing by 5σ. The corresponding weighted mean of the postshock pressures for the east is (regions 6, 7, and 9) $8.31 \pm 0.64 \times 10^{-10}$ erg cm^{-3} and, for the center and west (regions 1, 2, 4 and 5) is $8.64 \pm 0.36 \times 10^{-10}$ erg cm^{-3}. Thus, the mean postshock pressure for the central and western regions is within 1σ of that for the eastern regions, whereas the mean rim pressure for the eastern lobe is almost 3σ higher than the mean postshock pressure.

6. Discussion

6.1. Cocoon and Lobe Pressures

As discussed in Section 5.1, the postshock pressures are consistent with the single value of $8.6 \pm 0.3 \times 10^{-10}$ erg cm^{-3}. This value agrees well with the weighted mean of the independent rim pressures, $8.7 \pm 0.2 \times 10^{-10}$ erg cm^{-3} (Section 5.2). These values are also consistent with the weighted mean of the rim pressures for the central and western parts of the cocoon, $8.4 \pm 0.2 \times 10^{-10}$ erg cm^{-3}, but about 20% lower than the weighted mean of the rim pressures for the eastern region of the cocoon, $10.4 \pm 0.4 \times 10^{-10}$ erg cm^{-3}. In most shock models, the shocked gas undergoes rapid adiabatic expansion immediately behind the shock, so that, if anything, we should expect the rim pressures to be lower than the postshock pressures, suggesting that our estimates of the postshock pressures may be low (as discussed in Section 5.2). However, the relative narrowness of the rim of shock-compressed gas in Cyg A indicates that the rim gas is moving at a substantial fraction of the shock speed and so does not expand much behind the shock (see Section 4.4).

The rim pressures of Section 5.2 should provide the best measure of the pressure within the radio lobes of Cyg A. The rims lie immediately adjacent to the lobes, where the sound speed is expected to be high, so they should have very similar pressures. These pressure estimates rely almost solely on the assumption that the cocoon is axially symmetric. Although this is unlikely to be exact, the density estimates scale as the reciprocal of the square root of the depth of the emitting regions, making them insensitive to modest departures from the assumed geometry. If, for example, the high surface brightness of the rims in regions 6 and 9 (Figure 5) was due to the lobe cross-section being elliptical rather than circular, the ellipse would need to have an axial ratio of $\simeq$1.53. Although this cannot be ruled out, it is implausible. The brightness of the rims in regions 6 and 9 shows that the density there is almost certainly higher than in the other parts of the rim, and the 20% difference between the pressure of the western lobe and the rest of the cocoon is unlikely to be due to systematic error.

Such a large pressure difference is difficult to explain. The results of Section 6.6 support the widely held assumption that the sound speed in the lobes is much greater than the sound speed in the ICM, hence the speed of the cocoon shock. This should mean that the pressure within the lobes is nearly uniform away from the hotspots. Although the merger shock is overrunning the cluster core, it is also slow compared to the sound speed in the lobes and should have very little impact on the pressure gradients within the lobe.

In regions away from the hotspots, flow speeds within the lobes are generally low compared to the sound speed of the radio plasma. Thus, we expect the plasma pressure to be relatively uniform away from the immediate vicinity of the hotspots (Mathews & Guo 2010; Chon et al. 2012). Our pressure measurements confirm this expectation, at least to the level of ≃20%. We do not see evidence for higher pressures in the outer parts of the cocoon, close to the hotspots. However, our pressure measurements are sparse and less accurate in these regions (where densities are lower and the radius of curvature of the cocoon is smaller, reducing the brightness contrast of the shock fronts).

Although the shock in region 8 is projected only 7.6 kpc beyond the eastern hotspots, it cannot be associated directly with a hotspot. The pressure in the radio lobes is expected to be highest in the hotspots, so we expect the scale of the associated shock to be comparable to the small size of the hotspot. As a result, thermal emission from a hotspot shock will be very difficult to separate from its strong nonthermal X-ray emission. The extent of the shock in region 8 is too large for it to be part of the terminal jet shock. Its speed is also too slow to be directly associated with the hotspot (Table 2 and Section 6.4). This raises the issue of how the shock in region 8 can be projected beyond the hotspot, when its speed is significantly slower than the rate of advance of the hotspot. The most likely explanation is that the shock in region 8 is a transient feature. During most of its history, a hotspot would have led the expansion to the east, as it does now to the west. However, as they shift around in three dimensions, at times the hotspots can be projected behind the projected leading edge of the shock (see Section 6.4).

6.2. Motion of the AGN Relative to the Gas

Brightest cluster galaxies (BCGs) typically move at speeds exceeding 100 km s^{-1} with respect to their cluster hosts (Lauer et al. 2014). Continuing merger activity also disturbs the hot ICM, setting it in motion with respect to the cluster potential at speeds comparable to the BCG or greater (Ascasibar & Markevitch 2006; Randall et al. 2011). From Table 2, the distance from the AGN to the near part of the shock front to the north of the AGN in Cyg A is 32.9 kpc, while the distance to the shock front to the south is 41.0 kpc. Combining the Mach numbers from Table 2 with the deprojected preshock temperatures, the speeds of the shocks in regions 1 and 5 are 1500 km s^{-1} and 1670 km s^{-1}, respectively. The observed difference in shock strengths may be due to the higher ICM density and pressure to the north, as shown in Figure 4. Assuming that the average speed of separation of the shock fronts is constant at the current rate of 3170 km s^{-1}, it would have taken ≃2.28×10^7 years for the shocks to reach their current separation. In that time, the southern front has moved 8.1 kpc farther from the AGN than the northern one, with a mean speed 348 km s^{-1} faster than the northern shock. At the outset, when the shock fronts were close together, we assume that the state of the ICM outside the shock front was the same to the north and south, so that the two shocks had the same speeds. If the shock speeds varied linearly with time, then the average difference in the shock speeds would have been 85 km s^{-1}. Attributing the remainder of the north–south asymmetry to the motion northward, perpendicular to the cocoon axis, of the AGN, its northward velocity would equal half of the remaining difference in the speeds, i.e., 130 km s^{-1}.

The projected distances to the eastern shock and the western shock are 63.1 kpc and 74.3 kpc, respectively, so that the western shock is 11.2 kpc farther from the AGN than the eastern one. For the age estimate above, this gives a mean speed difference along the cocoon axis projected onto the plane of the sky of 480 km s^{-1}. As we lack an estimate for the difference in the shock speeds in this direction, we attribute the entire difference to the motion of the AGN through the gas, giving an eastward velocity along the axis of 240 km s^{-1}.

In the absence of a detailed model for the expansion history of the lobes and hotspots, there is substantial systematic uncertainty in both components of the estimated velocity. In particular, asymmetries in the ICM pressure distribution can affect the shock speed. We therefore estimate a total AGN speed of ≃270 km s^{-1} with respect to the gas, with a total systematic uncertainty of a factor of ∼2. Our projected speed is consistent with the proper motion estimates from Steenbrugge et al. (2014).

6.3. Outburst Energy and Power

Scaling the spherical hydrodynamic shock model to match the data enables all properties of the model to be expressed in physical units. Doing this for the northern and southern shocks in the central region (regions 1 and 5) provides two estimates for the age and energy of the outburst driving the cocoon shock. These regions were used as uncertainty in the geometry of the shock front is minimized where it is almost spherical. The temperature and density of the unshocked gas at radii of 40 kpc for the north and 45 kpc for the south were obtained from the deprojected profiles. For the northern shock, the age of the outburst was found to be $t_{\rm N} = 1.87 \times 10^7$ years, with a total energy of $E_{\rm N} = 6.67 \times 10^{59}$ erg. For the southern shock, the age was $t_{\rm S} = 1.84 \times 10^7$ years and the total energy $E_{\rm S} = 1.68 \times 10^{60}$ erg, a factor of ∼2.5 higher than for the north. Averaging the results produces a mean outburst age for the cocoon shock of $t_{\rm avg} = 1.86 \times 10^7$ years, with a total energy of $E_{\rm avg} = 1.17 \times 10^{60}$ erg.

Most of the difference between the two energy estimates is due to the difference in the volumes of the northern and southern shocked regions. From Table 2, the southern shock radius is ≃25% larger than the northern shock radius. In the spherically symmetric hydrodynamic model, this makes the volume enclosed by the southern shock almost twice that enclosed by the northern shock. All other things being equal, it would mean that the southern shock requires twice as much energy. As argued in Section 6.2, the AGN is moving northward through the ICM, exaggerating the apparent difference in the shock radii. Assuming that the outburst originates midway between the two shocks, rather than at the current location of the AGN, reduces the difference in outburst energy to ≃30%, with a comparable average energy to the original value. Much of the remaining energy difference can be attributed to the greater strength of the southern shock.

Additional uncertainty is present in the energy calculations because the volume of the spherical central region significantly underestimates the total volume of the shocked cocoon. A sphere of diameter equal to the distance from the northern shock to the southern shock has a volume of ≃2.08×10^5 kpc^3. Assuming axial symmetry, we have estimated the volume of the shocked cocoon by measuring its width perpendicular to the cocoon axis at many positions along the axis. Treating the cocoon as a stack of sections of cones, its

volume can be approximated as the sum of the section volumes. Assuming that the cocoon axis is inclined 55° to our line of sight, we correct for projection by boosting the result by a factor of $1/\sin 55^\circ$ to obtain a total volume of 4.08×10^5 kpc^3. Given that the pressure within the lobes is approximately uniform (Sections 5.1 and 5.2), the total shock energy will have been underestimated by a factor close to the ratio of this volume to that of the spherical central region, or $\simeq 2$.

A further shortcoming of our hydrodynamic model is that the outburst is assumed to inject all of its energy explosively in a single, initial event. This is unrealistic. As discussed in Forman et al. (2017), the history of energy release determines what fraction of the energy resides in the lobes. This is minimized in a single explosive outburst, which is clearly ruled out for the lobes and cavities of Cyg A. If the energy were deposited at a constant rate instead, approximately twice as much energy would be required to obtain the same shock strength (Hardcastle & Krause 2013; English et al. 2016). In the absence of a more detailed model, we assume that the outburst power has been roughly constant, so that the total energy estimate needs to be boosted by a further factor of $\simeq 2$ over the value from the explosive hydrodynamic model. Putting the corrections together, we expect that we have underestimated the total outburst energy by a factor of $\simeq 4$. The systematic error in this is unlikely to exceed a factor of 2. Thus, we estimate the total outburst energy after correction to be $\simeq 4.7 \times 10^{60}$ erg.

For a given outburst energy, the explosive shock model maximizes the shock speed at all times, minimizing the estimated outburst age. A model with constant jet power would produce slower shocks at early times, although the shock speed would still decrease with time. Assuming that the shock speed is constant at its present value provides the likely upper limits on the outburst age of 2.34×10^7 years and 2.51×10^7 years for the northern and southern shocks, respectively. Therefore, the age estimates from the explosive shock model are unlikely to be low by more than a factor of $\simeq 1.3$. Combining the total energy estimate of 4.7×10^{60} erg with the upper and lower age estimates gives estimates for the time-averaged outburst power in the range 0.6–0.8 $\times 10^{46}$ erg s^{-1}, in broad agreement with other estimates (Carilli & Barthel 1996; Wilson et al. 2006; Godfrey & Shabala 2013). We use the value of 10^{46} erg s^{-1}, with a systematic uncertainty of a factor of 2, as representative of the mean outburst power below. Although the jet power, lobe, and ICM pressures of Cyg A are high compared to those of the more typical FRII galaxies in the sample of Ineson et al. (2017), its dimensionless properties, such as the pressure ratios and the cocoon shock Mach numbers, are typical.

6.4. Hotspot Speeds

We can make a geometric estimate for the speed of advance of each hotspot. If the axis of the cocoon is inclined 55° to our line of sight, the deprojected distance from the AGN to the shock near the tip of the eastern (western) jet is a factor of $\simeq 2.1$ ($\simeq 2.5$) greater than the average distance from the AGN to the shock fronts in regions 1 and 5 (Table 2). Multiplying these factors by the average speed of the advance for the innermost shocks provides estimates of the time-averaged speeds of the outermost parts of the cocoon shock. Using an average shock speed in regions 1 and 5 of 1590 ± 50 km s^{-1}, the recession speed of the eastern hotspot is 3340 ± 110 km s^{-1} and that of the western hotspot is 3980 ± 130 km s^{-1}. Using the deprojected temperature of 6.42 ± 0.27 keV gives a Mach number of 2.54 ± 0.14 for the shock near the eastern hotspot. With a deprojected temperature of 9.25 ± 0.49 keV, the Mach number near the western hotspot is 2.52 ± 0.16.

The estimated shock speeds fall well short of the hotspot speeds. In part, the shock speeds may be underestimated (Section 6.1), but the shape of the shock front is also critical. We may use a self-similar model to demonstrate that this behavior is consistent with a shock geometry that tapers toward the hotspots. We assume that the shape of the cocoon shock remains fixed as it expands. Although this is an idealization, the changes in relative speed that cause departures from self-similarity generally occur on timescales comparable to the age of an outburst, so we should not expect to find large departures from self-similar expansion in practice. If the size of the front is proportional to $g(t)$, where t is the time, its shape projected onto the sky can be defined as a level surface of a function of two arguments, in the form $f[x/g(t), y/g(t)] = 0$, where the AGN is located at $x = y = 0$. Since the shock velocity is perpendicular to the level surfaces of f, the speed of the shock at any position on the front is given by

$$v = \frac{1}{g}\frac{dg}{dt}\frac{|\boldsymbol{r}\cdot\nabla f|}{|\nabla f|} = \frac{v_0}{r_0} r\cos\theta, \tag{6}$$

where θ is the angle between the radius vector and the normal to the front, so that $\cos\theta = \boldsymbol{r}\cdot\nabla f/(r|\nabla f|)$. In the second form, values are referred to the position on the front closest to the AGN, where $r = r_0(t)$, $v = v_0(t)$, and the radius vector $\boldsymbol{r}$ must be perpendicular to the front, so that $\cos\theta = 1$. This expression determines how the shock speed depends on position at a fixed time. Alternatively, the shape of the front may be specified by giving x and y as functions of a parameter s and then, from Equation (6), the expansion speed varies over the front as

$$v \propto r\cos\theta = \frac{|y\,dx/ds - x\,dy/ds|}{\sqrt{(dx/ds)^2 + (dy/ds)^2}}. \tag{7}$$

Clearly, the expansion speed is the same at every point on a spherical front (circular on the sky). It is also constant for a conical front of the form $y = y_0 - \eta x$, with constant η (Equation (7)). From Figure 1, the cocoon shock of Cyg A may be roughly approximated as a sphere, capped to the east and west by a pair of opposed cones. If the cones are tangent where they attach to the sphere, the expansion speed of the self-similar front would be constant everywhere but at the tips of the two cones. Although this is a crude model for the cocoon shock of Cyg A, it illustrates how the shock speed can be substantially less than the speed of the hotspots, except in small regions close to the hotspots.

6.5. Hotspot Pressures

Rather than drilling into the ICM at a single location at the tip of the cocoon, hotspots shift around rapidly (Scheuer 1982; Williams & Gull 1985), so that we expect the mean speed of the shock at the tip to be significantly lower than the instantaneous speed of the hotspot. Therefore, using the mean speed of the shock at the tip of the cocoon to estimate the hotspot pressure should provide a minimum estimate, $p_{\rm hs,min}$. Using the value of the external pressure at its deprojected distance of 77.0 kpc from the AGN with the hotspot Mach number (Section 6.4), the pressure required to drive the eastern hotspot needs to be at least $p_{\rm hs,min,E} = 1.48 \pm 0.32 \times 10^{-9}$ erg cm^{-3}. For the western

hotspot, at a deprojected distance of 90.7 kpc, this calculation gives $p_{\rm hs,min,W} = 1.28 \pm 0.33 \times 10^{-9}$ erg cm^{-3}.

Synchrotron self-Compton (SSC) models for the radio and X-ray emission of the hotspots can provide more realistic estimates of the hotspot pressures (Harris et al. 1994). Decomposing the pressure into a sum of contributions from the magnetic field, electrons, and nonradiating particles, it may be expressed as $p_{\rm hs} = p_B + p_{\rm e} + p_{\rm n}$. To relate this to the results of the SSC model, we recast it as

$$p_{\rm hs} = \frac{U_B}{3}\left[\frac{3p_B}{U_B} + \frac{U_{\rm e}}{U_B}\left(1 + \frac{p_{\rm n}}{p_{\rm e}}\right)\right], \quad (8)$$

where U_B is the magnetic energy density, $U_{\rm e}$ is the electron energy density, and we have assumed that $p_{\rm e} = U_{\rm e}/3$ (tending to underestimate the electron pressure for $\Gamma_{\rm min} \to 1$). Under the simplest assumptions, the magnetic field is isotropic, so that the magnetic pressure is related to the magnetic energy density by $p_B = U_B/3$, giving

$$p_{\rm hs} = \frac{U_B}{3}\left[1 + \frac{U_e}{U_B}\left(1 + \frac{p_{\rm n}}{p_{\rm e}}\right)\right]. \quad (9)$$

For a light jet, electrons and positrons contribute equally to the "electron" pressure, $p_{\rm e}$, while the pressure of the nonradiating particles is negligible. For a matter-dominated jet, the number density of nonradiating particles (ions) in the hotspot will be comparable to the electron density. Their relative pressures then depend on the particle energy distributions, which are determined by acceleration mechanisms. The simplest assumption would be $p_n/p_e = 1$, but the acceleration mechanisms can also make the ion pressure substantially greater than the electron pressure (Malkov & Drury 2001), so that the total hotspot pressure may be substantially greater than our estimates below. If the magnetic field is well-ordered, the effective magnetic pressure could also be up to a factor of 3 greater. Higher hotspot pressures would entail greater instantaneous hotspot speeds and larger mass fluxes through the jets (see below and Section 6.6).

From their SSC model for the radio and X-ray emission of the bright eastern hotspot (D), Stawarz et al. (2007) found $B = 270\ \mu$G, with values of $U_{\rm e}/U_B$ in the range 3–4. Adopting $U_{\rm e}/U_B = 3.5$ as representative, Equation (9) gives pressures of $p_{\rm hs,E} = 4.4 \times 10^{-9}$ erg cm^{-3} for a light jet, or $p_{\rm hs,E} = 7.7 \times 10^{-9}$ erg cm^{-3} for a matter-dominated jet with $p_{\rm n} = p_{\rm e}$. Similarly, using $U_{\rm e}/U_B = 7.5$ and $B = 170\ \mu$G for the western hotspot (A) gives corresponding pressures of $p_{\rm hs,W} = 3.3 \times 10^{-9}$ erg cm^{-3} or 6.1×10^{-9} erg cm^{-3}. Bearing in mind the substantial systematic uncertainties, these values are consistent with expectations. For the two SSC pressure estimates above, the eastern hotspot would drive shocks at Mach $\simeq$4.3 or 5.7 into the ICM, both significantly faster than the estimated mean Mach number of 2.54, as anticipated. For the western hotspot, the SSC pressures would drive shocks at Mach $\simeq$4.0 or 5.4, also both substantially faster than the mean Mach number of 2.52.

These arguments relate values that may vary on widely differing timescales. Jet fluxes are observed to change on timescales ranging upward from the light-crossing time of the jet (e.g., Harris et al. 2006). The hotspots of Cyg A are compact, with radii of $\simeq$1 kpc, and they are composed of gas that is likely to be relativistic (or nearly so), so they can respond to rapid changes in the confining pressure on timescales ranging upward from a few thousand years. If the jet axis of Cyg A is inclined 55° to our line of sight, its western hotspots are $\simeq$100 kpc closer to us than its eastern hotspots, so that the light travel time from the western hotspots is $\simeq$0.3 Myr longer (the delay may be partly offset by the greater distance from the AGN to the western hotspots, but only orders of magnitude matter here). The eastern jet of Cyg A has a filamentary appearance, with what appear to be twists over scales of several kiloparsecs (Perley et al. 1984), suggesting it moves about on a timescale of several thousand years (if the jet is relativistic). Thus, variations in jet power or direction could cause the hotspot pressures determined from the SSC model to vary on timescales more than an order of magnitude shorter than the light travel delay between the eastern and western hotspots. By contrast, we have used the shock speed near the tips of jets averaged over the duration of the outburst, about 20 Myr (Section 6.3), for the other pressure estimates. Given the disparity of the timescales, the consistency between the various pressure estimates is, perhaps, fortuitous. It implies that the "current" values of the jet power at both hotspots are comparable to the mean power averaged over the lifetime of the outburst.

6.6. Jet and Hotspot Composition

The power and pressure estimates can be used to estimate some properties of the jets. Given the substantial systematic uncertainty, we employ a one-dimensional, steady, relativistic flow model (Landau & Lifshitz 1959; Laing & Bridle 2002). The flow rate of rest mass through the jet is given by

$$\dot{M} = \rho A c \beta \gamma, \quad (10)$$

where ρ is the proper density of the rest mass, A is the cross-sectional area of the jet, the bulk flow speed is $v = \beta c$, and γ is the corresponding Lorentz factor. The jet power can be expressed as

$$P_{\rm j} = (\gamma - 1)\dot{M}c^2 + hAc\beta\gamma^2, \quad (11)$$

where the enthalpy per unit volume is related to the pressure by $h = \Gamma p/(\Gamma - 1)$, and the ratio of specific heats of the jet fluid, Γ, is assumed to be constant. The total momentum flux, or thrust, of the jet is given by

$$\Pi = (P_{\rm j}/c + \dot{M}c)\beta. \quad (12)$$

For both hotspot A and hotspot D, the SSC pressure estimate of Section 6.5 significantly exceeds our estimate of the static pressure in the lobe. Assuming that the excess pressure in a hotspot is due to the ram pressure of the jet, we have

$$\Pi = (p_{\rm hs} - p)A_{hs}, \quad (13)$$

where $A_{\rm hs}$ is the hotspot cross-sectional area. Although neither A nor D is a "primary" hotspot (Carilli & Barthel 1996), each is the largest and brightest in its lobe and so provides the greatest estimates for the jet thrust. This estimate would decrease under adiabatic expansion, so that, if the hotspot is no longer confined by the jet, our estimate of the jet thrust will be low, causing the mass flow rates to be underestimated. Using Equation (11) to

eliminate $\dot{M}$ in Equation (12) then yields

$$\frac{P_{\rm j}}{\Pi c} = \frac{\beta\gamma}{\gamma+1} + \frac{hA}{\Pi}\beta\gamma, \tag{14}$$

and this can be solved for the flow speed using the estimates above.

For each lobe, we use the SSC estimates of the hotspot pressure for $p_{\rm n} = 0$ and for $p_{\rm n} = p_{\rm e}$ (Section 6.5). For the static pressure in each jet, we use the lobe pressure estimated from the averaged rim pressure (Section 5.2). The jet power was taken to be one-half of the mean total outburst power, so we use $P_{\rm j} = 5 \times 10^{45}$ erg s^{-1} as a representative value (Section 6.3). However, the minimum jet thrust would then exceed the thrust estimated from the hotspot pressure for the lower hotspot pressure in each lobe (for $p_{\rm n} = 0$). For those cases, the jet power was reduced to the maximum value consistent with the hotspot pressure,

$$P_{\rm j,max} = c\sqrt{(\Pi + hA)\Pi}\,, \tag{15}$$

which makes $\dot{M} = 0$.

The higher hotspot pressure estimates were obtained under the assumption that the nonradiating particles contribute as much to the hotspot pressure as the electrons, in which case we should expect the hotspot, hence also the jet, to be matter dominated. For the model parameters discussed here, the equivalent temperatures of the jet ($kT_{\rm j} = \mu m_{\rm H} p/\rho$) fall in the MeV to GeV range, so the electrons would be relativistic and most of the ions nonrelativistic, making the ratio of specific heats for the jet close to $\Gamma = 13/9$. By contrast, to obtain the lower hotspot pressures, the pressure of the nonradiating particles in the hotspot is assumed to be negligible. This implies the jet has a negligible ion content, with positrons as the predominant positive charges. Such a jet is light, and the majority of particles in it will be relativistic, making $\Gamma = 4/3$ (Krause 2003, 2005; Guo & Mathews 2011). Kino et al. (2012) found both heavy and light jet models to be consistent with prior Cyg A observations, albeit with a preference for light jets, and so we considered both models in our analysis.

Since the jet widths are difficult to assess from the 5 GHz radio map, we relate them to the hotspot sizes. In both the X-ray and 5 GHz radio images, we estimate the FWHMs of hotspots A and D to be 2.4 kpc and 2.0 kpc, respectively. If the jet covers the whole of each hotspot, the corresponding jet radii would be about 1.2 kpc in the west and 1.0 kpc in the east. A jet may also be narrower than its hotspot, confining it by the dentist drill effect (Scheuer 1982). To keep it confined, the moving tip of the jet must then traverse the whole hotspot within the few thousand years required for the hotspot to expand significantly. From Section 6.5, the twisted appearance of the eastern jet suggests it moves on a timescale of several thousand years. To keep the hotspots confined, we therefore assume that the jet radius needs to be at least half that of the hotspot, and so we use jet radii equal to 0.5 or 1 times the radius of the hotspot.

The two jet radii and two hotspot pressures for each lobe, with their accompanying jet powers and equations of state discussed above, give the eight sets of model parameters and results listed in Table 4. The four matter-dominated heavy jet models give jet speeds in the range $\beta = 0.61$–0.88, while those for the light jet models are in the range $\beta = 0.65$–0.87. These are comparable to VLBI speeds measured in the core (Krichbaum et al. 1998; Boccardi et al. 2016), although the large uncertainties in the powers and areas of the jets would allow almost any speed $\gtrsim 0.15c$ (jet speeds with large γ requiring much smaller jet areas). For the light jet models, the jet powers, reduced to be consistent with the hotspot pressures (Equation (15)), lie in the range 3.4–4.9 $\times 10^{45}$ erg s^{-1}, comfortably in agreement with the results of Section 6.3. Our results do not rule out light, matter-dominated jets (with a higher hotspot pressure, $P_{\rm j} \simeq P_{\rm j,max}$, and $\Gamma = 4/3$), although they would require powers of 6.5–8.7 $\times 10^{45}$ erg s^{-1}, stretching the upper limit of the acceptable power range at the higher end. Jet speed is an increasing function of the power and a decreasing function of the thrust and jet area. For the matter-dominated models, the sound speeds in the jet ranges from 0.38–0.45 c and the jet Mach numbers from 1.5–2.2. For the light jet models in the table, the sound speed is $c/\sqrt{3}$, and the range of Mach numbers is 1.13–1.50.

Considering only models with jet speeds comparable to the VLBI speeds, the kinetic power fraction, $(\gamma - 1)\dot{M}c^2/P_{\rm j}$, is modest. For example, the matter-dominated models of Table 4 have kinetic power fractions $\lesssim$50%. As defined here, the kinetic power fraction of the light jet models is zero, since $\dot{M} = 0$. Restricting attention to these models eliminates the poorly constrained parameter $\dot{M}$, while still yielding properties consistent with our observations. The jet power for the light jet models is $P_{\rm j,max}$ (Equation (15)), which is determined by the other model parameters. It is most sensitive to our estimate of the hotspot pressure and somewhat less sensitive to the jet pressure and area. The resulting jet powers are consistent with the estimates from Section 6.3 and the corresponding jet speeds,

$$\beta = \sqrt{\frac{\Pi}{\Pi + hA}}\,, \tag{16}$$

are also in the range expected.

The jets of Cyg A may well have entrained some ordinary matter. For example, assuming they are old, the stars of Cyg A would shed roughly $5 \times 10^{-5}\,M_\odot$ yr^{-1} within the volume of each jet. If all of this is entrained, it would contribute $\dot{M}c^2 \simeq 3 \times 10^{42}$ erg s^{-1} to each jet, three orders of magnitude smaller than the jet power. From Equations (11) and (12), this amount of entrained gas would only have an appreciable impact on the flow for $\gamma \gtrsim 1000$. For $\gamma \sim 1$, unless the mass entrained by the jets is about three orders of magnitude greater, the jets may be treated as light. Since light jet models provide flow solutions that are consistent with the observed properties of Cyg A, these results favor the jets being light.

7. Conclusions

Deep *Chandra* observations of the cocoon shock of Cyg A were analyzed to quantify physical properties of the AGN outburst, the lobes, and the jets of Cyg A. X-ray surface brightness profiles of the shocks were used to determine shock strengths in a number of regions around the cocoon. Fitting the profiles with a hydrodynamic model for the AGN outburst gave Mach numbers for the cocoon shock in the range 1.18–1.66. The outburst energy for the system was determined to be $\simeq 4.7 \times 10^{60}$ erg, after substantial corrections, and the outburst age was found to be $\simeq 2 \times 10^7$ years, giving a mean outburst power of $P \simeq 10^{46}$ erg s^{-1}, with a systematic uncertainty of about a factor of 2. The mean power is consistent with

Table 4
Sample Jet Model Parameters

Jet	P_j[a] (10^{45} erg s^{-1})	Γ	p (10^{-9} erg cm^{-3})	p_{hs}	r_j[b] (kpc)	β	$\dot{M}$ ($M_\odot$ yr^{-1})	f_{KE}[c]	kT_j[d] (MeV)	s/c[e]
East	5	13/9	1.04	7.7	1.0	0.667	0.070	0.27	118	0.438
East	5	13/9	1.04	7.7	0.5	0.882	0.031	0.40	137	0.455
East	4.51	4/3	1.04	4.4	1.0	0.668	0	0	⋯	0.577
East	3.45	4/3	1.04	4.4	0.5	0.874	0	0	⋯	0.577
West	5	13/9	0.84	6.1	1.2	0.608	0.109	0.32	75	0.385
West	5	13/9	0.84	6.1	0.6	0.835	0.055	0.51	73	0.382
West	4.89	4/3	0.84	3.3	1.2	0.650	0	0	⋯	0.577
West	3.68	4/3	0.84	3.3	0.6	0.863	0	0	⋯	0.577

Notes.
[a] Jet power is reduced below 5×10^{45} erg s^{-1} in cases where the minimum thrust exceeds the thrust estimated from the hotspot pressure. The resulting maximum value makes $\dot{M} = 0$.
[b] Jet area is $A = \pi r_j^2$.
[c] Kinetic power fraction is $(\gamma - 1)\dot{M}c^2/P_j$.
[d] Equivalent jet temperature for matter-dominated models, $kT_j = \mu m_H p/\rho$, with ρ from Equation (10).
[e] Sound speed from the Synge model for hydrogen plasma at temperature kT_j for matter-dominated models and $c/\sqrt{3}$ for light jet models.

independent estimates of the outburst power for Cyg A based on simulations of radio and X-ray emissions.

The off-center location of the AGN with respect to the cocoon shock indicates that it is moving through the ICM. From the shock speeds and age, the AGN (i.e., the BCG) is estimated to be moving at 270 km s^{-1} with respect to the gas, with a substantial systematic uncertainty.

Spectra of regions in the thin rim of compressed gas between the radio lobes and the shocks were used to estimate pressures. The mean rim pressure agrees well with the postshock pressures determined from the shock jump conditions. The rim pressure for the western lobe, $8.4 \pm 0.2 \times 10^{-10}$ erg cm^{-3}, is ∼20% lower than the mean value for the remainder of the cocoon, $10.4 \pm 0.4 \times 10^{-10}$ erg cm^{-3}. The rim pressures provide good estimates of the pressure within the radio lobes, apart from the vicinity of the hotspots. They show some evidence for persistence of a 20% pressure difference between the east and the west, which is puzzling given the high sound speed expected in the lobes. Despite this, one of our main findings is that the pressure is uniform within ∼20% throughout the bulk of the cocoon.

Scaling by distance from the AGN, we estimate the Mach numbers of the shocks near the hotspots of Cyg A to be 2.54 ± 0.14 in the east and 2.52 ± 0.16 in the west, significantly greater than any Mach number obtained by fitting the cocoon shock. A simple geometric model shows that the shock speed need only be so high in a small region close to the hotspots. The speed of the shock front near the hotspots places lower limits on the hotspot pressures of $p_{hs,min,E} = 1.48 \pm 0.32 \times 10^{-9}$ erg cm^{-3} in the east and $p_{hs,min,W} = 1.28 \pm 0.33 \times 10^{-9}$ erg cm^{-3} in the west. These values are higher than the estimated cocoon pressure but are significantly lower than the hotspot pressures estimated from SSC models. This is consistent with positions of the hotspots moving about on the cocoon shock over time. The SSC-derived hotspot pressures show that the ram pressures of the jets are at least twice as large as their static pressures.

Estimates of the jet power and hotspot pressures were used with a steady, one-dimensional, matter-dominated flow model to determine jet properties. These models are consistent with mildly relativistic flow speeds within the allowed parameter ranges. Notably, light jet models, which carry a negligible flux of rest mass and so have one less parameter than the general model, agree with the observed properties of the jets and hotspots. This result favors the jets of Cyg A being light, meaning that both the momentum flux and kinetic power due to the flow of rest mass through the jets are negligible compared to those due to the flow of internal energy.

Support for this work was provided by the National Aeronautics and Space Administration through *Chandra* Award Number GO5-16117A issued by the *Chandra* X-ray Observatory Center, which is operated by the Smithsonian Astrophysical Observatory for and on behalf of the National Aeronautics Space Administration under contract NAS8-03060. P.E.J.N. was supported in part by NASA contract NAS8-03060.

Software: CIAO v4.9 (Fruscione et al. 2006), XSPEC 12.9.1h (Arnaud 1996).

ORCID iDs

Bradford Snios https://orcid.org/0000-0002-4900-928X
Paul E. J. Nulsen https://orcid.org/0000-0003-0297-4493
Mark Birkinshaw https://orcid.org/0000-0002-1858-277X
Diana M. Worrall https://orcid.org/0000-0002-1516-0336
Ralph P. Kraft https://orcid.org/0000-0002-0765-0511
Brian R. McNamara https://orcid.org/0000-0002-2622-2627
Chris Carilli https://orcid.org/0000-0001-6647-3861
Alastair C. Edge https://orcid.org/0000-0002-3398-6916
Richard A. Perley https://orcid.org/0000-0001-7097-8360

References

Anders, E., & Grevesse, N. 1989, GeCoA, 53, 197
Arnaud, K. A. 1996, in ASP Conf. Ser. 101, Astronomical Data Analysis Software and Systems V, ed. G. H. Jacoby & J. Barnes (San Francisco, CA: ASP), 17
Ascasibar, Y., & Markevitch, M. 2006, ApJ, 650, 102
Bartel, N., Sorathia, B., Bietenholz, M. F., Carilli, C. L., & Diamond, P. 1995, PNAS, 92, 11371
Begelman, M. C., Blandford, R. D., & Rees, M. J. 1984, RvMP, 56, 255
Bîrzan, L., Rafferty, D. A., McNamara, B. R., Wise, M. W., & Nulsen, P. E. J. 2004, ApJ, 607, 800

Blundell, K. M., Rawlings, S., & Willott, C. J. 1999, AJ, 117, 677
Boccardi, B., Krichbaum, T. P., Bach, U., et al. 2016, A&A, 585, A33
Bower, R. G., Benson, A. J., Malbon, R., et al. 2006, MNRAS, 370, 645
Carilli, C. L., & Barthel, P. D. 1996, A&ARv, 7, 1
Carilli, C. L., Perley, R. A., & Dreher, J. H. 1988, ApJL, 334, L73
Carilli, C. L., Perley, R. A., & Harris, D. E. 1994, MNRAS, 270, 173
Chon, G., Böhringer, H., Krause, M., & Trümper, J. 2012, A&A, 545, L3
Croton, D. J., Springel, V., White, S. D. M., et al. 2006, MNRAS, 365, 11
de Vries, M. N., Wise, M. W., Huppenkothen, D., et al. 2018, MNRAS, submitted
Dickey, J. M., & Lockman, F. J. 1990, ARA&A, 28, 215
Duffy, R. T., Worrall, D. M., Birkinshaw, M., et al. 2018, MNRAS, in press
Dunn, R. J. H., & Fabian, A. C. 2006, MNRAS, 373, 959
English, W., Hardcastle, M. J., & Krause, M. G. H. 2016, MNRAS, 461, 2025
Fabian, A. C. 1994, ARA&A, 32, 277
Fabian, A. C. 2012, ARA&A, 50, 455
Fanaroff, B. L., & Riley, J. M. 1974, MNRAS, 167, 31
Forman, W., Churazov, E., Jones, C., et al. 2017, ApJ, 844, 122
Forman, W., Jones, C., Churazov, E., et al. 2007, ApJ, 665, 1057
Fruscione, A., McDowell, J. C., Allen, G. E., et al. 2006, Proc. SPIE, 6270, 62701V
Godfrey, L. E. H., & Shabala, S. S. 2013, ApJ, 767, 12
Guo, F., & Mathews, W. G. 2011, ApJ, 728, 121
Hardcastle, M. J., & Croston, J. H. 2010, MNRAS, 404, 2018
Hardcastle, M. J., & Krause, M. G. H. 2013, MNRAS, 430, 174
Harris, D. E., Carilli, C. L., & Perley, R. A. 1994, Natur, 367, 713
Harris, D. E., Cheung, C. C., Biretta, J. A., et al. 2006, ApJ, 640, 211
Heinz, S., Brüggen, M., Young, A., & Levesque, E. 2006, MNRAS, 373, L65
Heinz, S., Reynolds, C. S., & Begelman, M. C. 1998, ApJ, 501, 126
Hinshaw, G., Larson, D., Komatsu, E., et al. 2013, ApJS, 208, 19
Ineson, J., Croston, J. H., Hardcastle, M. J., & Mingo, B. 2017, MNRAS, 467, 1586
Kalberla, P. M. W., Burton, W. B., Hartmann, D., et al. 2005, A&A, 440, 775
Kino, M., Kawakatu, N., & Takahara, F. 2012, ApJ, 751, 101
Krause, M. 2003, A&A, 398, 113
Krause, M. 2005, A&A, 431, 45
Krichbaum, T. P., Alef, W., Witzel, A., et al. 1998, A&A, 329, 873
Laing, R. A., & Bridle, A. H. 2002, MNRAS, 336, 1161
Landau, L. D., & Lifshitz, E. M. 1959, Fluid Mechanics (Oxford: Pergamon)
Lauer, T. R., Postman, M., Strauss, M. A., Graves, G. J., & Chisari, N. E. 2014, ApJ, 797, 82
Ledlow, M. J., Owen, F. N., & Miller, N. A. 2005, AJ, 130, 47
Malkov, M. A., & Drury, L. O. 2001, RPPh, 64, 429
Mathews, W. G., & Guo, F. 2010, ApJ, 725, 1440
Mathews, W. G., & Guo, F. 2012, ApJ, 755, 13
McNamara, B. R., & Nulsen, P. E. J. 2007, ARA&A, 45, 117
Mendygral, P. J., Jones, T. W., & Dolag, K. 2012, ApJ, 750, 166
Nulsen, P. E. J., Hambrick, D. C., McNamara, B. R., et al. 2005, ApJL, 625, L9
Nulsen, P. E. J., Li, Z., Forman, W. R., et al. 2013, ApJ, 775, 117
Nulsen, P. E. J., Powell, S. L., & Vikhlinin, A. 2010, ApJ, 722, 55
Owen, F. N., Ledlow, M. J., Morrison, G. E., & Hill, J. M. 1997, ApJL, 488, L15
Perley, R. A., Dreher, J. W., & Cowan, J. J. 1984, ApJL, 285, L35
Rafferty, D. A., McNamara, B. R., Nulsen, P. E. J., & Wise, M. W. 2006, ApJ, 652, 216
Randall, S. W., Forman, W. R., Giacintucci, S., et al. 2011, ApJ, 726, 86
Reynolds, C. S., Heinz, S., & Begelman, M. C. 2001, ApJL, 549, L179
Scheuer, P. A. G. 1974, MNRAS, 166, 513
Scheuer, P. A. G. 1982, in IAU Symp. 97, Extragalactic Radio Sources, ed. D. S. Heeschen & C. M. Wade (Cambridge: Cambridge Univ. Press), 163
Smith, D. A., Wilson, A. S., Arnaud, K. A., Terashima, Y., & Young, A. J. 2002, ApJ, 565, 195
Stawarz, L., Cheung, C. C., Harris, D. E., & Ostrowski, M. 2007, ApJ, 662, 213
Steenbrugge, K. C., Blundell, K. M., & Pyrzas, S. 2014, A&A, 563, A131
Tabor, G., & Binney, J. 1993, MNRAS, 263, 323
Tucker, W., & David, L. P. 1997, ApJ, 484, 602
Vestergaard, M., & Barthel, P. D. 1993, AJ, 105, 456
Williams, A. G., & Gull, S. F. 1985, Natur, 313, 34
Wilson, A. S., Smith, D. A., & Young, A. J. 2006, ApJL, 644, L9
Yaji, Y., Tashiro, M. S., Isobe, N., et al. 2010, ApJ, 714, 37